Atomic-scale Characterization of Dilute Dopants in Topological Insulators via STEM-EDS Using Registration and Unit Cell Averaging Techniques

Min-Chul Kang,[1] Farhan Islam,[1,2] Jiaqiang Yan,[3] David Vaknin,[1] Robert J. McQueeney,[1,3] Ping Lu,[4] Lin Zhou[1,5*]

[1] Ames National Laboratory, Ames, Iowa 50011, USA

[2] Department of Physics and Astronomy, Iowa State University, Ames, IA 50011, USA

[3] Materials Science and Technology Division, Oak Ridge National Laboratory, Oak Ridge, TN 37831, USA

[4] Sandia National Laboratories, Albuquerque, New Mexico 87185, USA

[5] Department of Materials Science and Engineering, Iowa State University, IA, 50011, USA

*Corresponding author: linzhou@ameslab.gov

Abstract

Magnetic dopants in three-dimensional topological insulators (TIs) offer a promising avenue for realizing the quantum anomalous Hall effect (QAHE) without the necessity for an external magnetic field. Understanding the relationship between site occupancy of magnetic dopant elements and their effect on macroscopic property is crucial for controlling QAHE. By combining atomic-scale energy-dispersive X-ray spectroscopy (EDS) maps obtained by aberration-corrected scanning transmission electron microscopy (AC-STEM) and novel data processing methodologies, including semi-automatic lattice averaging and frame registration, we have determined the substitutional sites of Mn atoms within the 1.2% Mn doped Sb_2Te_3 crystal. More importantly, the methodology developed in this study extends beyond Mn-doped Sb_2Te_3 to other quantum materials, traditional semiconductors, and even electron irradiation sensitive materials.

Keywords

Dilute magnet, atomic-scale EDS mapping, aberration-corrected scanning transmission electron microscopy (AC-STEM), Lattice averaging, Non-rigid frame registration

1. Introduction

Since the discovery of the quantized Hall effect (Klitzing et al., 1980; Tsui et al., 1982), there has been a suggestion to utilize the quantum anomalous Hall effect (QAHE) in three-dimensional topological insulators (TIs) by adding magnetic elements, which eliminates the need for an external magnetic field (Onoda & Nagaosa, 2003; Liu et al., 2008; Yu et al., 2010; Qiao et al., 2010; Chang et al., 2013). This concept inspired the interest in introducing collective ferromagnetic alignment of various magnetic defects to induce symmetry breaking and cause the quantized conductance and lossless transport effects, which hold promising applications in quantum computing(Kitaev, 2006, 2003) and dilute magnetic semiconductors (Ohno et al., 1999; Awschalom & Flatté, 2007; Betthausen et al., 2014; Dyck et al., 2002).

One representative way of controlling magnetic defects is doping of transition metal elements, which could change the local magnetic moments of quantum materials. Therefore, determining the occupant site of magnetic dopant elements and the effect on macroscopic properties is crucial for controlling QAHE(Yu et al., 2010). Recent studies have delved into the electronic band structures and local magnetic moments of three-dimensional TIs, such as Sb_2Te_3 and Bi_2Te_3, using transition metal elements as dopants, including V, Cr, Fe, and Mn(Kandala et al., 2015; Bestwick et al., 2015; Islam et al., 2023; Yu et al., 2010; Wimmer et al., 2021). Some research has also predicted substitution positions of these dopants using density functional theory simulations (Zhang et al., 2013; Islam et al., 2018; Chang et al., 2013; Checkelsky et al., 2014; Kou et al., 2014; Wimmer et al., 2021).

Interestingly, QAHE has been experimentally observed in Cr- and V-doped $(Bi, Sb)_2Te_3$ but not in Mn-doped counterparts (Chang et al., 2023). Recent studies on Mn-substituted Sb_2Te_3 have shown the prevalence of strong antiferromagnetic Mn-Mn dimers, which may

interfere with producing a ferromagnetic state, thus hindering the development of QAHE (Islam et al., 2023). However, further real-space exploration of Mn-doped Sb_2Te_3 to confirm this prediction are still limited.

The doping of transition metal elements in TIs takes place at the atomic-scale, requiring high-resolution technique for analysis. Scanning transmission electron microscopy (STEM) with energy dispersive X-ray spectroscopy (EDS) and electron energy loss spectroscopy (EELS) has been commonly used to directly observe the chemical distribution of dopants. The first atomic-resolution chemical analysis using STEM was achieved through EELS (Browning et al., 1993), providing superior spatial resolution as it is mainly influenced by the probe size of electron beam itself. However, challenges arise with detecting elements like antimony (atomic number 51) and tellurium (atomic number 52), which are common in 3D TIs, as their delayed maximum form of the EELS edge peak overlap, making it difficult to distinguish signals from each other. Additionally, the signal-to-background ratio of EELS is relatively poor, thus it is hard to detect elements with low concentration.

On the other hand, with the development of aberration corrected STEM, STEM-EDS becomes more and more widely used for atomic-scale chemistry analysis due to it high signal-to-background ratio and mitigated fluorescence and spread of X-rays in thin specimen (Dellby et al., 2001; Batson et al., 2002; Chu et al., 2010; d'Alfonso et al., 2010). Therefore, most research on dopant studies in chalcogenide, including TIs has been conducted using STEM-EDS (Volykhov et al., 2021; Vladimirova et al., 2023; Tominaga, 2019; Zheng et al., 2019; Wang et al., 2019; Kim et al., 2021). Nevertheless, EDS typically has low collection efficiency and requires extended data acquisition times, especially as the dopant concentration decreases (Kim et al., 2021). Prolonged sample exposure time to electron beam can lead to beam induced damage, requiring analysis with

relatively thick samples to preserve atomic crystal structures. However, utilization of a thick sample can introduce the delocalization effect because of electron channeling and de-channeling events during electron transmission through the sample. The EDS signals could no longer be localized to atomic columns, leading to loss of the spatial resolution (Feng et al., 2018; Lugg et al., 2015; Oxley et al., 1999; Chen et al., 2016; Spurgeon et al., 2017; Lu et al., 2018). This trade-off of using the thin and thick specimen is illustrated schematically in Figure S1.

Achieving optimal signal-to-noise ratio (SNR) with sufficiently thin samples requires collecting signals over a larger area and integrating signals to increase signal density. This signal integration is called for registration, which is classically studied from computer science (Brown, 1992). This registration was first applied to high resolution TEM in 1990th (Möbus & Rühle, 1994; Schweinfest et al., 1999). Recent work about effort to improve the SNR of atomic-scale EDS map has led to a lattice-averaged approach in which the EDS maps that are related by lattice translation vectors are averaged (Lu et al., 2018, 2014). The lattice translation vectors in the approach are typically defined by the projected unit cell in the beam direction (Lu et al., 2014). More recently, similar works have demonstrated the use of these techniques in different contexts (Yankovich et al., 2016; Wenner et al., 2017).

These unit cell averaging, and registration techniques have been applied in various studies to enhance signal quality in electron microscopy images (Kohno et al., 2022; Susarla et al., 2022). However, it is still challenging to acquire atomic resolution data for elements with low concentration inside the materials. Our study differentiates itself by focusing on low signal and introduces a novel approach that integrates semi-automated repeatability searches and non-rigid registration to improve the SNR. This method allows for seamless integration of registration and unit cell averaging, providing advantages in investigating the distribution of dilute dopants.

In this study, we present a new registration solution for utilizing atomic-scale STEM- EDS mapping for determination of dopant site in the low concentration doped TIs. We demonstrated this method in a 1.2% Mn doped Sb_2Te_3 and determined the Mn dopants occupy substitutionally at Sb sites in the crystal. Our approach is similar to the previous method, wherein the lattice-averaging is used to improve the SNR. However, it differs in the aspect that the translation vectors are determined automatically by an image processing code, and a sub-unit cell in the projected structure is allowed to increase the number of averages that can be carried out from a single EDS map. In addition, our method combines EDS maps obtained from different thin regions using a frame registration method to further improve SNR. The approach that combines EDS maps from the different regions can be potentially useful for the study of electron-beam sensitive materials, as the EDS map from each region can be acquired within a short acquisition time scale, thus mitigating irradiation damage.

2. Materials and Methods

The Sb_2Te_3 crystal has a rhombohedral crystalline structure ($R\bar{3}m$), which has quintuple layers divided by van der Waals gap along *c* direction, as illustrated in Figure 1 (a). Mn-doped Sb_2Te_3 single crystals were grown by Bridgman technique. Sb shots (Alfa Aesar, 99.9999%), Te shots (Alfa Aesar, 99.9999%), and Mn pieces (Alfa Aesar, 99.99%) were used as starting materials, weighted in the desired molar ratio, and loaded into the quartz ampoule. The ampoule was then sealed under a dynamic vacuum. The growth was performed in a home-made Bridgman furnace. (Islam et al., 2023; May et al., 2020). The furnace was first heated to 800 °C, kept at this temperature for 24 hours to get a uniform melt, cooled down to 680 °C at a cooling rate of 0.5 °C/h. After dwelling at 680 °C for 3 days, the furnace was powered off. The 1.2% Mn doped Sb_2Te_3 TEM sample was prepared using focused ion beam (FIB, FEI Helios NanoLab G3). STEM

imaging and EDS data was taken from a Titan Themis with Super-X detector with 18 mrad convergence angle and 200 kV. The specific X-ray energy spectrum data set was obtained with a 512×512 pixels frame at a pixel size of ~10 pm, an electron probe size of ~100 pm, probe current of 80 pA, 150 frames and a total acquisition time of 30 minutes. EDS map was background subtracted with Velox software (Thermo Fisher Scientific Inc.). STEM-HAADF images and EDS maps of Te, Sb, and Mn taken under [100] and [120] ZA are shown in Figure 1 (b-e) and (f-i), respectively. Because the atomic percentage of Mn is only ~1.2 at% in the sample, making it impossible to detect the Mn atom position in raw data. Further increasing of data acquisition time (tens of hours, if the sample is stable enough) is required to collect enough signal and reduce Poisson noise, as the basic relationship between SNR and signal count (N) follows:

$$SNR\ (Poisson\ noise) \propto \sqrt{N} \qquad \text{(eq.1)}$$

To maximize the SNR, a new data processing methods based on (1) lattice averaging of single EDS map using semi-automatic processing routine and (2) combining EDS maps from multiple regions using frame registration method were developed. The methods and their improvements are shown schematically in Figure 2. The details are described in the following.

2.1 Lattice averaging

Atomic-scale EDS elemental mapping with lattice averaging has been demonstrated previously (Lu et al., 2014). In this method, a small portion of EDS map is translated to equivalent positions in the map, and the EDS counts within these regions are added to enhance the SNR. The degree of SNR improvement depends on the number of average (N_a) that can be carried out and can be maximized by choosing the smallest translation vectors, often determined by the projected unit cell (Figure 2 (b)). For materials with large unit cells such as Sb_2Te_3 crystal, N_a can be

relatively small, limiting the SNR improvement by this technique. In that case, employing a sub-unit cell may be useful if the projected cell possesses certain symmetry. An example is illustrated in Figure 2 (c), showing increase of N_a by choosing a sub-cell. The sub-cell determination is done semi-automatically in our approach.

The auto lattice-averaging method is described as follows. We start with identifying the two translation vectors that define periodicity of the images. In general, two translation vectors require 4 variables since each vector has an x- and y- component in a STEM image. During our data acquisition, we aligned one lattice (atomic row) plane with the fast-scanning direction which is normally called for x-direction, this leaves us with three independent variables to determine: the *x*-repeating size (r_x), the *y*-repeating size (r_y), and the lane-by-lane step (r_w), as shown in Figure 3(a).

The process of finding out the three variable starts with r_x. To determine the r_x value, we set the r_y value to the total y pixel size of the image while adjusting the r_x value. The criterion for selecting the optimal r_x value is defined by Equation (2).

$$\arg\max_{r_x}\left(\frac{\max(\sum I)-\min(\sum I)}{\max(\sum I)}\right) \quad \text{(eq.2)}$$

Where, "I" represents the matrix of image segments for lattice averaging, and "$\sum I$" denotes the result of lattice averaging, which is the integrated matrix of segmented matrices "I". The maximum and minimum intensities of the image matrix are denoted by "max" and "min", respectively. The relative difference is calculated by normalizing "$\sum I$" by its maximum value which is set to be 1. The r_x that maximize the parentheses value in Equation (2) is the r_x value for the following lattice averaging calculation. The process for identifying the other variables, r_y, and r_w, follows a similar approach.

Figure 3 illustrates the automated process using the criteria in Equation (2) to identify appropriate *r* values (r_x, r_y and r_w) for lattice averaging, using a sample image made of the lattice with a Gaussian distribution intensity at the lattice point. In this example, the value in Equation (2) has a local maximum at the multiple of 104 pixels, giving rise to r_x of 104 pixels (Figure 3(b)). Deviations from this appropriate value result in a blurred image due to improper overlap, as shown in Figure 3 (e). Criterion of r_y shows the global maximum at 204 pixel indicates the exact unit cell size, whereas the local maximum at 102 pixel, serves effectively as a sub-unit cell size. With the calculated r_x and r_y values, the final variable, r_w can be determined to 52, which represents lane-by-lane step size.

Additionally, since dopants can sometimes substitute specific positions and form superlattices (Gudiksen et al., 2002; Cargnello et al., 2015), lattice averaging with the sub-unit or unit cell determined using STEM as outlined above can potentially yield inaccurate information of dopant structure due to the relatively insignificant dopant contribution to STEM image intensity. This issue can be mitigated by conducting lattice averaging with sizes that are multiples of the semi-automatically detected cell for validation. The example process is described in Figure S3.

2.2 Frame registration

The frame registration method combining the EDS maps acquired from different regions, involves calculating the relative displacement between different images using cross-correlation (Savitzky et al., 2018). However, scanning conditions and sample drifting, when acquiring EDS maps from different regions may fluctuate over time, leading to variable scanning distortion and drifts among images acquired, as illustrated in Figure 2(d). This drift can be classified as linear drift, non-linear drift, and random noise (Ophus et al., 2016). In the case of EDS, the dwelling time

of the electron probe is much longer than just STEM imaging, linear drift is got more severe than any other scanning drift. However, the rigid registration method, typically used in cross-correlations, might result in signal misplacement or blurring due to the linear drift (Figure 2(e)). To mitigate these issues, we use a non-rigid registration method, which accounts for both displacement and deformations within each image. This approach allows more accurate alignment between different images, accommodating scanning condition variations and sample drifting difference among the EDS maps. The extent of SNR improvement via frame registration is contingent upon the number of frames (N_f) registered, as shown in Figure 2(d-f).

Figure 4 illustrates the schematic process of the non-rigid registration method we used. The process starts with calculations of r_x, r_y and r_w for each image, and calibrating (or resizing) images with respect to the values of first image '*f*'. The r_x, r_y and r_w is calculated by process described in section 2.1. These values of the first image are recommended to be selected manually, to minimize the error induced by coincidental mismatch. And then, determine a range of r_x, r_y and r_w from first image with nearby local minimum of manually selected appropriate peak. And the other images are automatically calculated the r_x, r_y and r_w.

The "*n*-th" images' pixel, denoted as P_{x_n}, P_{y_n}, are resized using interpolation described in Equation 3. In this study, we use the Lanczos interpolation to reduce the aliasing during interpolation (Duchon, 1979). The process is shown schematically in Figure 4b.

$$P_{x_n} = P_x \times \frac{r_{x_1}}{r_{x_n}},\ P_{y_n} = P_y \times \frac{r_{y_1}}{r_{y_n}} \quad \text{(eq.3)}$$

In the case of r_w steps, primarily influenced by linear drift, images are optimized by de-shearing deformation using Equation 4, as depicted in Figure 4(c).

$$r_{w_1} \times \frac{P_y}{r_{y_1}} - r_{w_n} \times \frac{P_y}{r_{y_n}} \quad \text{(eq.4)}$$

Subsequently, the optimal displacement vector $\boldsymbol{\tau}(x_d, y_d)$ between the re-calibrated n-th images and first image *f* is determined (Figures 4 (d) and (e)) for frame registration, where x_{dn} and y_{dn} is the displacement value of the n-th image in *x* and *y* directions, with respect to the first frame. The optimal displacement value is achieved by employing an argument equation (Equation 5) through dynamically changing element of $\boldsymbol{\tau}$ (x_d, y_d) akin to the scanning process at the cross-correlation of two images (f ★ g), as described in previous research (Savitzky et al., 2018).

$$\arg\max_{\boldsymbol{\tau}(x_d, y_d)}((f \bigstar g)(\boldsymbol{\tau})) \quad \text{(eq.5)}$$

The outcomes of cross-correlation calculations for $\boldsymbol{\tau}(x_d, y_d)$ shifts are graphically represented in a three-dimensional plot, as seen in Figure 4(e). This method can deduce the displacement from each image, and the images are subsequently combined based on the determined x_{dn} and y_{dn}. While this cross-correlation method is much slower than the conventionally used FFT-based cross-correlation calculation, it provides better accuracy for atomic-scale image registration which include preventing lattice hop (Savitzky et al., 2018).

Consequently, the total signal count (N_{total}) accumulates as a product of the number of lattice averaging (N_a) and number of frames used in the frame registration (N_f). These two methods serve complementary to each other. For samples vulnerable to electron beam irradiation, acquiring the dataset from different areas for a short period and combining them using the registration method can alleviate the beam damage to the sample. Alternatively, for the samples with simple structures and are not sensitive to electron irradiation, lattice averaging using unit cell or sub-unit cells can help to reduce the overall acquisition time, and improve the SNR for the detection of low-concentration dopants. Example code for this comprehensive process is available in Appendix A.

3. Results and Discussion

3.1 Atomic-scale EDS maps using lattice-averaging method

The acquired HAADF images and EDS maps from Mn-doped Sb_2Te_3 are presented in Figure 5. The alternating layers of Te and Sb in the structure are clearly visible. However, the SNR is significantly lower in the Mn map due to its low atomic concentration, posing challenges in precisely determining its distribution in the crystal lattice. By applying the method outlined above (Figure 3) to analyze the HAADF image in Figure 5 (a), the values of r_x, r_y and r_w are determined to be 33, 91, and 21 pixels, respectively. These parameters are then utilized for lattice averaging analysis of the raw EDS elemental map. The processed results are displayed as insets in Figure 5 (a-d), revealing that the Mn dopants are primarily located at the Sb positions.

Since the HAADF image with 512 × 512 pixels (Figure 5 (a)) was divided into 33 segments with 33 × 91 pixels each, resulting in a 75-fold increase in the signal. Simple arithmetic based on Equation (1) reveals an improvement of $\sqrt{75}$ in the SNR. Observation on [120] ZA, as shown in Figure 5 (e-h), yield results similar to those in the [100] ZA, confirming the Mn substitutes the Sb position.

However, as described in section 2.1 and Figure S3, Mn can substitute specific positions and form superlattices. The method described in Figure S3 is used to verify the presence of superlattice formation from Mn substitutions in our sample. The size change of lattice averaging segment is applied in the horizontal direction along the van der Waals gap layers between each quintuple layer. Our analyzed results (Figure S4) confirm random distribution of Mn.

3.2 Further SNR enhancement by image registration

Combining multiple map datasets through the proposed non-rigid registration in addition to lattice averaging allows for a further increase of the SNR. Figure 6 demonstrates the results of non-rigid registration using the proposed method in Figure 4. Taking the first image as the reference map (Figure 6 (a)), its r_x, r_y and r_w values were compared with additional data obtained from another locations (Figure 6 (b)). As explained in the method section, r_x and r_y are rescaled by interpolation to adjust their sizes (red arrow of Figure 6 (c)), and r_w is optimized by applying shearing to deform the image (blue arrow of Figure 6 (c)). The resulted registered images is shown in Figure 6 (d), which has a higher SNR level than the individual images. The number of images that can be used for registration is unlimited, and more images yield higher SNR. The inset in Figure 6 (d) is from combination of 3 sets of data, resulting in an SNR increase by a factor of $\sqrt{3}$. The inset in Figure 6 (d) shows the further lattice-averaged results following the registered images, which gives an overall SNR improvement of $\sqrt{3} \times \sqrt{75} = \sqrt{225}$ times. The same registration process, followed by the lattice averaging applied to the [120] ZA image produced a higher SNR map data as well, as shown Figure 6 (e).

To demonstrate the applicability of our method in studying beam-sensitive materials, we acquired a series of 100 EDS maps from different regions with a short acquisition time and lower beam current. The acquisition time for each image with single frame is ~53 seconds with a probe current of ~ 40 pA and 200 µs of dwelling time to reduce the fraction of flyback time (Ortega et al., 2021; Mullarkey et al., 2022), while the acquisition time and beam current used in Figure 5 are 33 minutes and 80 pA, respectively. After applying our method of non-rigid registration to the 100 datasets and performing the lattice averaging, we obtained the maps shown in Figure 6 (f). The Mn map in Figure 6 (f) is identical to that in Figure 5 (h), which is obtained following the lattice

averaging from the map obtained after a long acquisition time. This result validates the proposed method of acquiring EDS maps with a short acquisition from many areas and combining them with registration method for beam sensitive materials applications.

3.3 The Meaning of the Mn Substitution Position

As described in the introduction part, the most common method to induce an internal magnetic field is by incorporating ferromagnetism in TIs through doping with transition metal elements. However, the doping concentration must be carefully balanced: it needs to be low enough to preserve the robustness of the TI and its properties yet high enough to induce ferromagnetism. Recent studies on Mn-substituted Sb_2Te_3 have shown the prevalence of strong antiferromagnetic Mn-Mn dimers, which may interfere with producing a ferromagnetic state, thus hindering the development of QAHE (Islam et al., 2023). Therefore, as in this study, further real-space exploration of Mn-doped Sb_2Te_3 is crucial.

Typically, Mn is known to substitute for the positions of Sb ions below a 15% concentration (Yan et al., 2019; Liu et al., 2021; Lai et al., 2021; Riberolles et al., 2021; Murakami et al., 2019; Du et al., 2021). However, substitutions of magnetic elements as dopants could have preferential substitution positions, leading to the formation of superlattices beyond the unit cell size of the original structure (Gudiksen et al., 2002; Cargnello et al., 2015; Sevinçli et al., 2008).

As shown in the superlattice verification part (Figure S4), Mn substitutes the Sb position uniformly at 1.2 at% concentration. Based on this experimental result, we can infer that Mn is distributed randomly in Sb positions. According to Islam et al., Mn atoms in Sb positions could form Mn-Mn dimers, influencing magnetic and electronic properties and inducing local magnetism (Islam et al., 2023). The random distribution of Mn atoms implies the random formation of Mn-

to-Mn distance of antiferromagnetic dimers, with varying interaction strengths across all Sb positions (Gudiksen et al., 2002; Cargnello et al., 2015; Sevinçli et al., 2008). So, additional techniques for controlling the substitution position of the Mn to Sb position will be helpful to control the QAHE of Sb_2Te_3. These characteristics make it a rich subject for continued research, with the potential to unlock new technological applications in electronics and quantum computing.

4. Conclusion

In conclusion, our study presents a method for identifying preferred atomic sites occupied by low-concentration dopants in TIs through a combination of atomic-scale STEM EDS mapping and data processing. Our approach combines the auto lattice averaging method for single image processing and frame registration, which merges images from multiple regions. The auto lattice averaging identifies the lattice translation vectors semi-automatically based on HAADF images, while frame registration utilizes the non-rigid registration methods to correct translation vectors for image linear drift. Though furthermore drift correction of random noise and non-linear drift could be more helpful for better image, we have successfully demonstrated the effectiveness of our approach in identifying the substitution of Mn atoms for Sb positions in a 1.2 at% Mn-doped Sb_2Te_3. Furthermore, our method holds potential for broader applications in studying low concentration dopants in other quantum materials and semiconductors, as well as chemical analysis of the beam-sensitive samples.

Acknowledgments

This work was supported, in part, by the U.S. Department of Energy, Office of Science, xxxx. LZ and MK acknowledge the support from the startup funding from Iowa State University. All electron microscopy and related work were performed using instruments in the Sensitive Instrument Facility in Ames National Laboratory. The Ames National Laboratory is operated for the U.S. Department of Energy by Iowa State University under Contract No. DE-AC02-07CH11358. P. L acknowledges the support from the Center for Integrated Nanotechnologies, an Office of Science User Facility operated for the U.S. Department of Energy (DOE) Office of Science by Los Alamos National Laboratory (contract 89233218NCA000001) and Sandia National Laboratories (contract DE-NA0003525). Sandia National Laboratories is a multiprogram laboratory managed and operated by National Technology and Engineering Solutions of Sandia, LLC, a wholly owned subsidiary of Honeywell International, Inc., for the U.S. Department of Energy's National Nuclear Security Administration under contract DE-NA0003525. This paper describes objective technical results and analysis. Any subjective views or opinions that might be expressed in the paper do not necessarily represent the views of the U.S. Department of Energy or the United States Government.

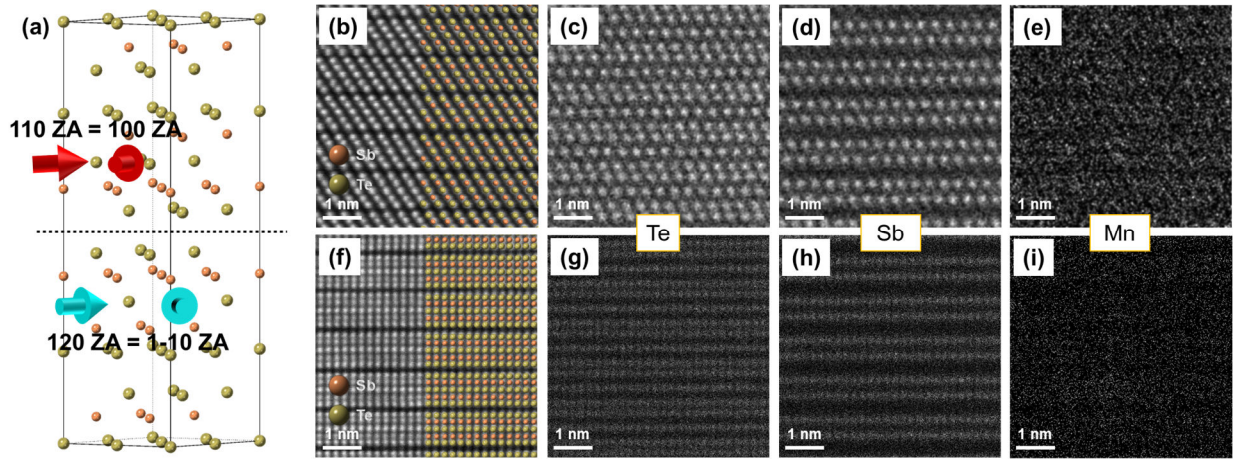

Fig 1. Overall structure of Sb_2Te_3 (a) Sb_2Te_3 structure drawn by Crystal maker software. (b, f) HAADF-STEM image of $(Sb_{0.97}Mn_{0.03})_2Te_3$ along [100] and [120] ZA, respectively. Inset is Sb_2Te_3 model of each ZA drawn by Crystal maker software. (c-e) Te, Sb and Mn elemental mapping along [100] ZA, respectively. (g-i) Te, Sb and Mn elemental mapping along [120] ZA, respectively.

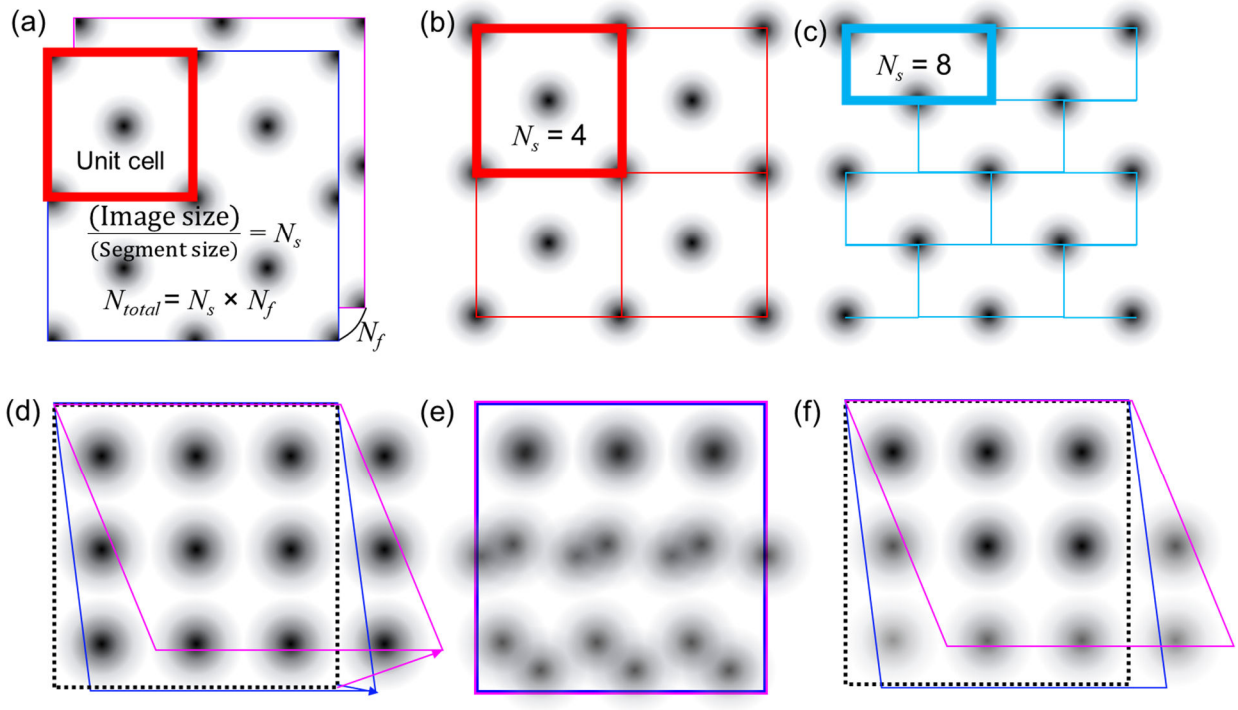

Fig 2. SNR improvements by lattice averaging and registration. (a) Combination of lattice averaging (increasing signal N_s times) and frame registration (increasing signal N_f times) for signal density (N_{total}) improvement. Schematic showing lattice averaging of (b) unit cell and (c) minimum repeating unit (sub-unit cell). (d) Ideal scanning at the exact same region (black dot line) and actual scanned region due to linear drift (blue and pink) before registration. Registration result from (e) rigid registration (only displacement calculated) and (f) non-rigid registration.

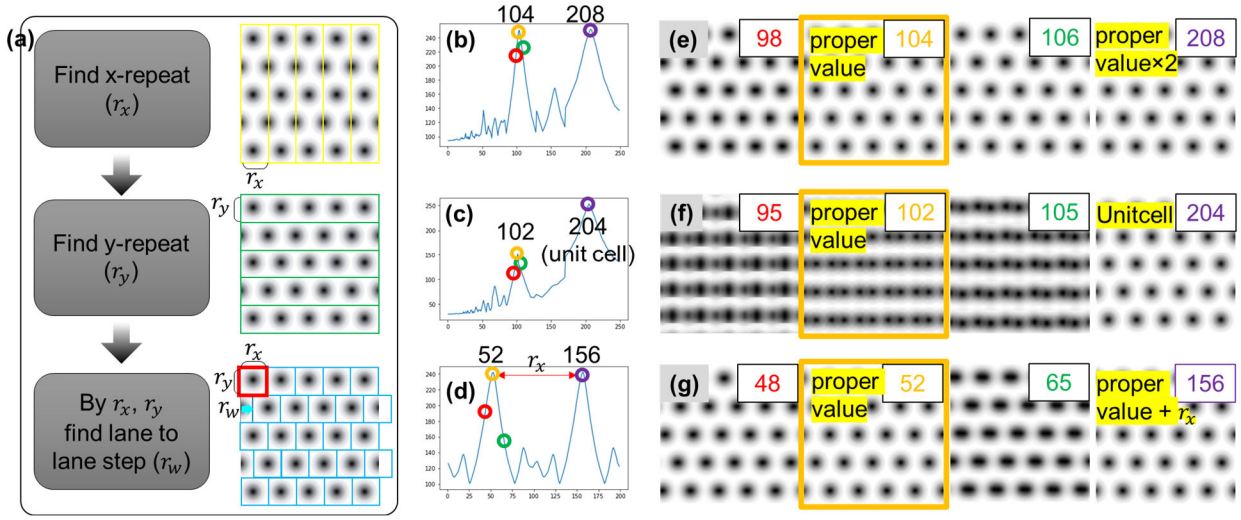

Fig 3. Schematic sequence of calculating r_x, r_y, r_w and lattice averaging. (a) Schematic of the automated process of finding repeating periods of periodically repeating gaussian mixture volume example. Change in criteria according to each variable (b) r_x, (c) r_y, (d) r_w and (e – g) lattice average results from each condition marked in (b – d), respectively.

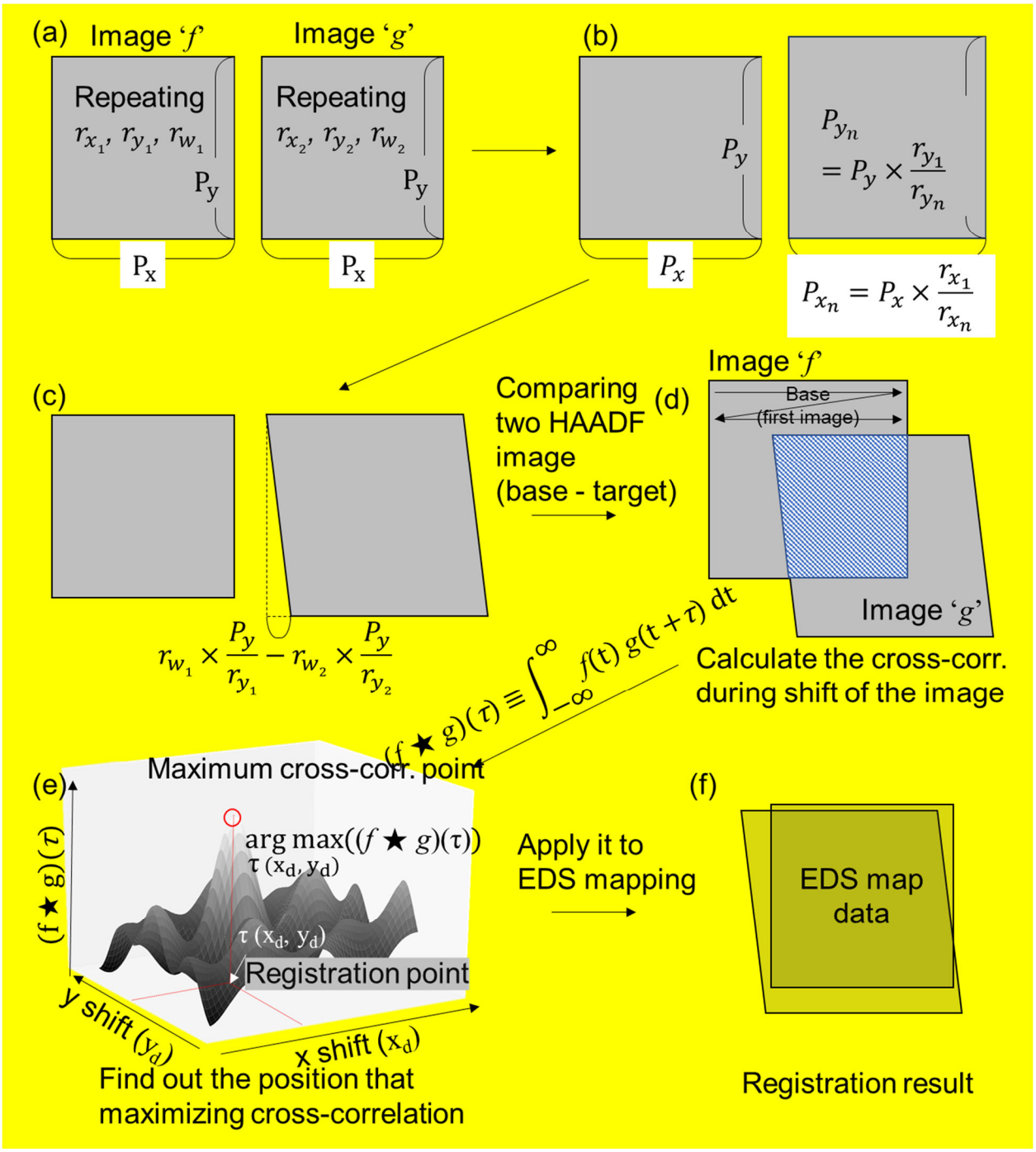

Fig 4. Schematic diagram of non-rigid registration method (a) Image '*f*' and '*g*' used for registration. (b) Resizing of image '*g*' with interpolation from (r_{x_1}, r_{y_1}) of image '*f*'. (c) Correcting shearing deformation by 'r_w' value. (d) Cross-correlation calculation with displacement $\boldsymbol{\tau}(x_d, y_d)$ between '*f*' and '*g*'. (e) Cross-correlation graph according to x shift (x_d) and y shift (y_d) (f) Result of EDS map registration.

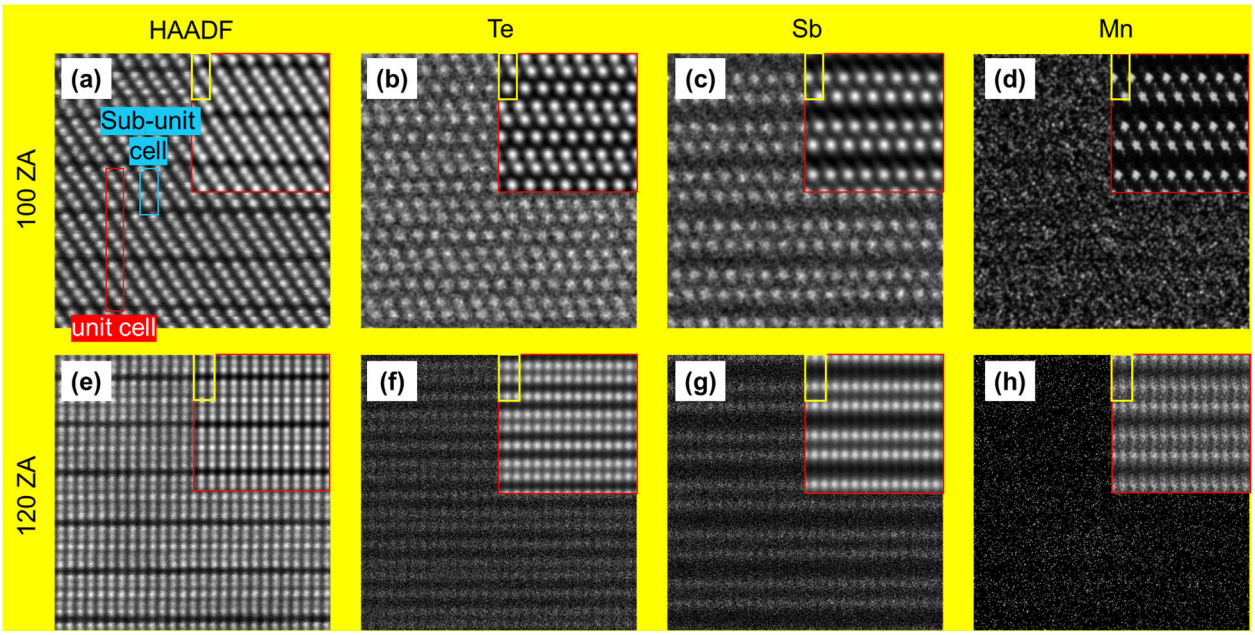

Fig 5. Comparing raw data and lattice averaging treated data (inset). HAADF-STEM image and elemental mapping from (a-d) [100] ZA and (e-h) [120] ZA. Note that the HAADF image and EDS map of $(Sb_{0.97}Mn_{0.03})_2Te_3$ shows significant difference of SNR. (The yellow square is unit cell size used in lattice averaging.)

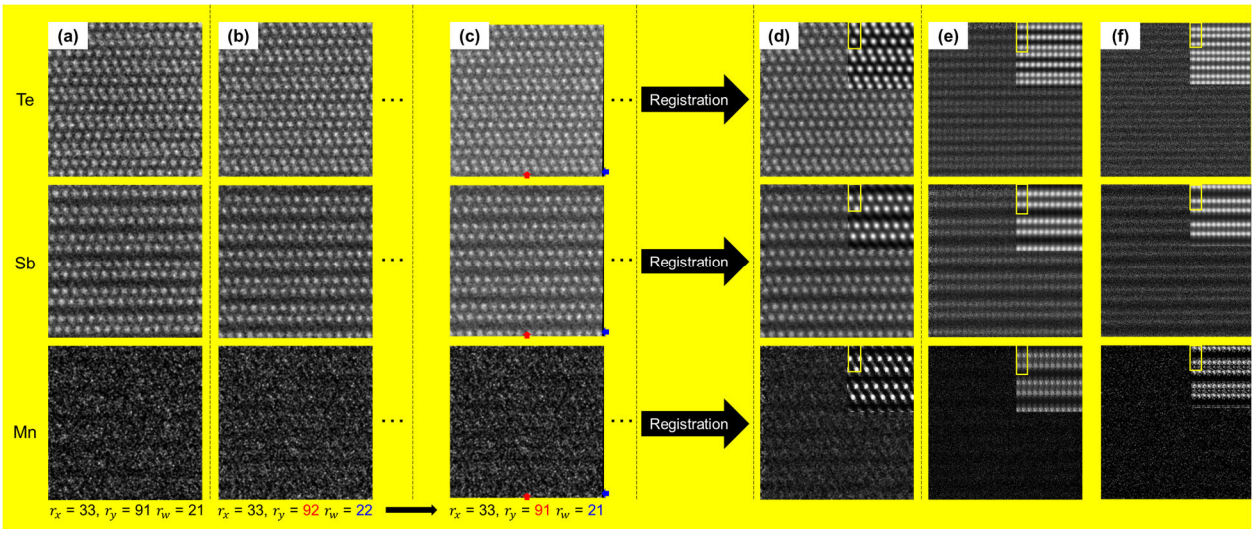

Fig 6. EDS map of 1.2% Mn doped Sb_2Te_3 after non-rigid registration. (a) reference map data, (b) additional map data, (c) optimized map data from (b), and (d) comparing the registration result and lattice averaging registration combined results (inset) along [100] ZA. (The yellow square is unit cell size used in lattice averaging.) (e) Comparing the registration result and lattice averaging combined results (inset) along [120] ZA. (f) Example of EDS mapping with shorter acquisition time and lower beam current to reduce electron beam damage. The conditions for this process are done with 100 images, 40 pA, 512 by 512 pixels and 200 µs dwelling time.

References

AWSCHALOM, D. D. & FLATTÉ, M. E. (2007). Challenges for semiconductor spintronics. *Nature physics* **3**, 153–159.

BATSON, P. E., DELLBY, N. & KRIVANEK, O. L. (2002). Sub-ångstrom resolution using aberration corrected electron optics. *Nature* **418**, 617–620.

BESTWICK, A. J., FOX, E. J., KOU, X., PAN, L., WANG, K. L. & GOLDHABER-GORDON, D. (2015). Precise quantization of the anomalous Hall effect near zero magnetic field. *Physical review letters* **114**, 187201.

BETTHAUSEN, C., GIUDICI, P., IANKILEVITCH, A., PREIS, C., KOLKOVSKY, V., WIATER, M., KARCZEWSKI, G., PIOT, B. A., KUNC, J. & POTEMSKI, M. (2014). Fractional quantum Hall effect in a dilute magnetic semiconductor. *Physical Review B* **90**, 115302.

BROWN, L. G. (1992). A survey of image registration techniques. *ACM computing surveys (CSUR)* **24**, 325–376.

BROWNING, N. D., CHISHOLM, M. F. & PENNYCOOK, S. J. (1993). Atomic-resolution chemical analysis using a scanning transmission electron microscope. *Nature* **366**, 143–146.

CARGNELLO, M., JOHNSTON-PECK, A. C., DIROLL, B. T., WONG, E., DATTA, B., DAMODHAR, D., DOAN-NGUYEN, V. V. T., HERZING, A. A., KAGAN, C. R. & MURRAY, C. B. (2015). Substitutional doping in nanocrystal superlattices. *Nature* **524**, 450–453.

CHANG, C.-Z., LIU, C.-X. & MACDONALD, A. H. (2023). Colloquium: Quantum anomalous hall effect. *Reviews of Modern Physics* **95**, 011002.

CHANG, C.-Z., ZHANG, J., FENG, X., SHEN, J., ZHANG, Z., GUO, M., LI, K., OU, Y., WEI, P. & WANG, L.-L. (2013). Experimental observation of the quantum anomalous Hall effect in a magnetic topological insulator. *Science* **340**, 167–170.

CHECKELSKY, J. G., YOSHIMI, R., TSUKAZAKI, A., TAKAHASHI, K. S., KOZUKA, Y., FALSON, J., KAWASAKI, M. & TOKURA, Y. (2014). Trajectory of the anomalous Hall effect towards the quantized state in a ferromagnetic topological insulator. *Nature Physics* **10**, 731–736.

CHEN, Z., WEYLAND, M., SANG, X., XU, W., DYCUS, J. H., LEBEAU, J. M., D'ALFONSO, A. J., ALLEN, L. J. & FINDLAY, S. D. (2016). Quantitative atomic resolution elemental mapping via absolute-scale energy dispersive X-ray spectroscopy. *Ultramicroscopy* **168**, 7–16.

CHU, M.-W., LIOU, S. C., CHANG, C.-P., CHOA, F.-S. & CHEN, C. H. (2010). Emergent chemical mapping at atomic-column resolution by energy-dispersive X-ray spectroscopy in an aberration-corrected electron microscope. *Physical review letters* **104**, 196101.

D'ALFONSO, A. J., FREITAG, B., KLENOV, D. & ALLEN, L. J. (2010). Atomic-resolution chemical mapping using energy-dispersive x-ray spectroscopy. *Physical Review B* **81**, 100101.

DELLBY, N., KRIVANEK, L., NELLIST, D., BATSON, E. & LUPINI, R. (2001). Progress in aberration-corrected scanning transmission electron microscopy. *Microscopy* **50**, 177–185.

DU, M., YAN, J., COOPER, V. R. & EISENBACH, M. (2021). Tuning fermi levels in intrinsic antiferromagnetic topological insulators MnBi2Te4 and MnBi4Te7 by defect engineering and chemical doping. *Advanced Functional Materials* **31**, 2006516.

DUCHON, C. E. (1979). Lanczos filtering in one and two dimensions. *Journal of Applied Meteorology and Climatology* **18**, 1016–1022.

DYCK, J. S., HÁJEK, P., LOŠŤÁK, P. & UHER, C. (2002). Diluted magnetic semiconductors based on Sb 2− x V x Te 3 (0.01<~ x<~ 0. 0 3). *Physical Review B* **65**, 115212.

FENG, B., LUGG, N. R., KUMAMOTO, A., SHIBATA, N. & IKUHARA, Y. (2018). On the quantitativeness of grain boundary chemistry using STEM EDS: A ZrO2 Σ9 model grain boundary case study. *Ultramicroscopy* **193**, 33–38.

GUDIKSEN, M. S., LAUHON, L. J., WANG, J., SMITH, D. C. & LIEBER, C. M. (2002). Growth of nanowire superlattice structures for nanoscale photonics and electronics. *nature* **415**, 617–620.

ISLAM, F., LEE, Y., PAJEROWSKI, D. M., OH, J., TIAN, W., ZHOU, L., YAN, J., KE, L., MCQUEENEY, R. J. & VAKNIN, D. (2023). Role of Magnetic Defects in Tuning Ground States of Magnetic Topological Insulators. *Advanced Materials* 2209951.

ISLAM, M. F., CANALI, C. M., PERTSOVA, A., BALATSKY, A., MAHATHA, S. K., CARBONE, C., BARLA, A., KOKH, K. A., TERESHCHENKO, O. E. & JIMÉNEZ, E. (2018). Systematics of electronic and magnetic properties in the transition metal doped Sb 2 Te 3 quantum anomalous Hall platform. *Physical Review B* **97**, 155429.

KANDALA, A., RICHARDELLA, A., KEMPINGER, S., LIU, C.-X. & SAMARTH, N. (2015). Giant anisotropic magnetoresistance in a quantum anomalous Hall insulator. *Nature communications* **6**, 7434.

KIM, Y.-M., LEE, K. H., FU, L., OH, M.-W., YANG, S.-H., NING, S., HAN, G., KIM, M. Y., KIM, J.-S. & JEONG, M. (2021). Atomic-scale chemical mapping of copper dopants in Bi2Te2. 7Se0. 3 thermoelectric alloy. *Materials Today Physics* **17**, 100347.

KITAEV, A. (2006). Anyons in an exactly solved model and beyond. *Annals of Physics* **321**, 2–111.

KITAEV, A. Y. (2003). Fault-tolerant quantum computation by anyons. *Annals of physics* **303**, 2–30.

KLITZING, K. V, DORDA, G. & PEPPER, M. (1980). New method for high-accuracy determination of the fine-structure constant based on quantized Hall resistance. *Physical review letters* **45**, 494.

KOHNO, Y., SEKI, T., FINDLAY, S. D., IKUHARA, Y. & SHIBATA, N. (2022). Real-space visualization of intrinsic magnetic fields of an antiferromagnet. *Nature* **602**, 234–239.

KOU, X., GUO, S.-T., FAN, Y., PAN, L., LANG, M., JIANG, Y., SHAO, Q., NIE, T., MURATA, K. & TANG, J. (2014). Scale-invariant quantum anomalous Hall effect in magnetic topological insulators beyond the two-dimensional limit. *Physical review letters* **113**, 137201.

LAI, Y., KE, L., YAN, J., MCDONALD, R. D. & MCQUEENEY, R. J. (2021). Defect-driven ferrimagnetism and hidden magnetization in MnBi 2 Te 4. *Physical Review B* **103**, 184429.

LIU, C.-X., QI, X.-L., DAI, X., FANG, Z. & ZHANG, S.-C. (2008). Quantum anomalous Hall effect in Hg 1− y Mn y Te quantum wells. *Physical review letters* **101**, 146802.

LIU, Y., WANG, L.-L., ZHENG, Q., HUANG, Z., WANG, X., CHI, M., WU, Y., CHAKOUMAKOS, B. C., MCGUIRE, M. A. & SALES, B. C. (2021). Site mixing for engineering magnetic topological insulators. *Physical Review X* **11**, 021033.

LU, P., MOYA, J. M., YUAN, R. & ZUO, J. M. (2018). Studies of x-ray localization and thickness dependence in atomic-scale elemental mapping by STEM energy-dispersive x-ray spectroscopy using single-frame scanning method. *Ultramicroscopy* **186**, 23–29.

LU, P., ZHOU, L., KRAMER, M. J. & SMITH, D. J. (2014). Atomic-scale chemical imaging and quantification of metallic alloy structures by energy-dispersive X-ray spectroscopy. *Scientific reports* **4**, 3945.

LUGG, N. R., KOTHLEITNER, G., SHIBATA, N. & IKUHARA, Y. (2015). On the quantitativeness of EDS STEM. *Ultramicroscopy* **151**, 150–159.

MAY, A. F., YAN, J. & MCGUIRE, M. A. (2020). A practical guide for crystal growth of van der Waals layered materials. *Journal of Applied Physics* **128**.

MÖBUS, G. & RÜHLE, M. (1994). Structure determination of metal-ceramic interfaces by numerical contrast evaluation of HRTEM micrographs. *Ultramicroscopy* **56**, 54–70.

MULLARKEY, T., PETERS, J. J. P., DOWNING, C. & JONES, L. (2022). Using your beam efficiently: Reducing electron dose in the STEM via flyback compensation. *Microscopy and Microanalysis* **28**, 1428–1436.

MURAKAMI, T., NAMBU, Y., KORETSUNE, T., XIANGYU, G., YAMAMOTO, T., BROWN, C. M. & KAGEYAMA, H. (2019). Realization of interlayer ferromagnetic interaction in MnS b 2 T e 4 toward the magnetic Weyl semimetal state. *Physical Review B* **100**, 195103.

OHNO, Y., YOUNG, D. K., BESCHOTEN, B. AL, MATSUKURA, F., OHNO, H. & AWSCHALOM, D. D. (1999). Electrical spin injection in a ferromagnetic semiconductor heterostructure. *Nature* **402**, 790–792.

ONODA, M. & NAGAOSA, N. (2003). Quantized anomalous Hall effect in two-dimensional ferromagnets: quantum Hall effect in metals. *Physical review letters* **90**, 206601.

OPHUS, C., CISTON, J. & NELSON, C. T. (2016). Correcting nonlinear drift distortion of scanning probe and scanning transmission electron microscopies from image pairs with orthogonal scan directions. *Ultramicroscopy* **162**, 1–9.

ORTEGA, E., NICHOLLS, D., BROWNING, N. D. & DE JONGE, N. (2021). High temporal-resolution scanning transmission electron microscopy using sparse-serpentine scan pathways. *Scientific reports* **11**, 22722.

OXLEY, M. P., ALLEN, L. J. & ROSSOUW, C. J. (1999). *Correction terms and approximations for atom location by channelling enhanced microanalysis*.

QIAO, Z., YANG, S. A., FENG, W., TSE, W.-K., DING, J., YAO, Y., WANG, J. & NIU, Q. (2010). Quantum anomalous Hall effect in graphene from Rashba and exchange effects. *Physical Review B* **82**, 161414.

RIBEROLLES, S. X. M., ZHANG, Q., GORDON, E., BUTCH, N. P., KE, L., YAN, J.-Q. & MCQUEENEY, R. J. (2021). Evolution of magnetic interactions in Sb-substituted MnBi 2 Te 4. *Physical Review B* **104**, 064401.

SAVITZKY, B. H., EL BAGGARI, I., CLEMENT, C. B., WAITE, E., GOODGE, B. H., BAEK, D. J., SHECKELTON, J. P., PASCO, C., NAIR, H., SCHREIBER, N. J., HOFFMAN, J., ADMASU, A. S., KIM, J., CHEONG, S. W., BHATTACHARYA, A., SCHLOM, D. G., MCQUEEN, T. M., HOVDEN, R. & KOURKOUTIS, L. F. (2018). Image registration of low signal-to-noise cryo-STEM data. *Ultramicroscopy* **191**, 56–65.

SCHWEINFEST, R., ERNST, F., WAGNER, T. & RÜHLE, M. (1999). High-precision assessment of interface lattice offset by quantitative HRTEM. *Journal of microscopy* **194**, 142–151.

SEVINÇLI, H., TOPSAKAL, M. & CIRACI, S. (2008). Superlattice structures of graphene-based armchair nanoribbons. *Physical Review B* **78**, 245402.

SPURGEON, S. R., DU, Y. & CHAMBERS, S. A. (2017). Measurement Error in Atomic-Scale Scanning Transmission Electron Microscopy-Energy-Dispersive X-Ray Spectroscopy (STEM-EDS) Mapping of a Model Oxide Interface. *Microscopy and Microanalysis* **23**, 513–517.

SUSARLA, S., NAIK, M. H., BLACH, D. D., ZIPFEL, J., TANIGUCHI, T., WATANABE, K., HUANG, L., RAMESH, R., DA JORNADA, F. H., LOUIE, S. G., ERCIUS, P. & RAJA, A. (2022). Hyperspectral imaging of exciton confinement within a moiré unit cell with a subnanometer electron probe. *Science* **378**, 1235–1239.

TOMINAGA, J. (2019). The Design and Application on Interfacial Phase-Change Memory. *physica status solidi (RRL)–Rapid Research Letters* **13**, 1800539.

TSUI, D. C., STORMER, H. L. & GOSSARD, A. C. (1982). Two-dimensional magnetotransport in the extreme quantum limit. *Physical Review Letters* **48**, 1559.

VLADIMIROVA, N. V, FROLOV, A. S., SÁNCHEZ-BARRIGA, J., CLARK, O. J., MATSUI, F., USACHOV, D. Y., MUNTWILER, M., CALLAERT, C., HADERMANN, J. & NEUDACHINA, V. S. (2023). Occupancy of lattice positions probed by X-ray photoelectron diffraction: A case study of tetradymite topological insulators. *Surfaces and Interfaces* **36**, 102516.

VOLYKHOV, A. A., FROLOV, A. S., NEUDACHINA, V. S., VLADIMIROVA, N. V, GERBER, E., CALLAERT, C., HADERMANN, J., KHMELEVSKY, N. O., KNOP-GERICKE, A. & SANCHEZ-BARRIGA, J. (2021). Impact of ordering on the reactivity of mixed crystals of topological insulators with anion substitution: Bi2SeTe2 and Sb2SeTe2. *Applied Surface Science* **541**, 148490.

WANG, J.-J., WANG, J., XU, Y., XIN, T., SONG, Z., POHLMANN, M., KAMINSKI, M., LU, L., DU, H. & JIA, C.-L. (2019). Layer-switching mechanisms in Sb2Te3. *physica status solidi (RRL)–Rapid Research Letters* **13**, 1900320.

WENNER, S., JONES, L., MARIOARA, C. D. & HOLMESTAD, R. (2017). Atomic-resolution chemical mapping of ordered precipitates in Al alloys using energy-dispersive X-ray spectroscopy. *Micron* **96**, 103–111.

WIMMER, S., SÁNCHEZ-BARRIGA, J., KÜPPERS, P., NEY, A., SCHIERLE, E., FREYSE, F., CAHA, O., MICHALIČKA, J., LIEBMANN, M. & PRIMETZHOFER, D. (2021). Mn-Rich MnSb2Te4: A topological insulator with magnetic gap closing at high curie temperatures of 45–50 K. *Advanced Materials* **33**, 2102935.

YAN, J.-Q., ZHANG, Q., HEITMANN, T., HUANG, Z., CHEN, K. Y., CHENG, J.-G., WU, W., VAKNIN, D., SALES, B. C. & MCQUEENEY, R. J. (2019). Crystal growth and magnetic structure of MnBi 2 Te 4. *Physical Review Materials* **3**, 064202.

YANKOVICH, A. B., ZHANG, C., OH, A., SLATER, T. J. A., AZOUGH, F., FREER, R., HAIGH, S. J., WILLETT, R. & VOYLES, P. M. (2016). Non-rigid registration and non-local principle component analysis to improve electron microscopy spectrum images. *Nanotechnology* **27**, 364001.

YU, R., ZHANG, W., ZHANG, H.-J., ZHANG, S.-C., DAI, X. & FANG, Z. (2010). Quantized anomalous Hall effect in magnetic topological insulators. *science* **329**, 61–64.

ZHANG, J.-M., MING, W., HUANG, Z., LIU, G.-B., KOU, X., FAN, Y., WANG, K. L. & YAO, Y. (2013). Stability, electronic, and magnetic properties of the magnetically doped topological insulators Bi 2 Se 3, Bi 2 Te 3, and Sb 2 Te 3. *Physical Review B* **88**, 235131.

ZHENG, Y., WANG, Y., XIN, T., CHENG, Y., HUANG, R., LIU, P., LUO, M., ZHANG, Z., LV, S. & SONG, Z. (2019). Direct atomic identification of cation migration induced gradual cubic-to-hexagonal phase transition in Ge2Sb2Te5. *Communications Chemistry* **2**, 13.